Nano Research
https://doi.org/10.1007/s12274-017-1962-z
Research Article
ISSN 1998-0124
CN 11-5974/O4

Piezo-phototronic and pyro-phototronic effects to enhance Cu(In, Ga)Se_2 thin film solar cells

Laipan Zhu[1], Pei Lin[1], Baodong Chen[1], Longfei Wang[1], Libo Chen[1], Ding Li[1], and Zhong Lin Wang[1,2] (✉)

[1] *Beijing Institute of Nanoenergy and Nanosystems, Chinese Academy of Sciences, Beijing 100083, China*
[2] *College of Nanoscience and Technology, University of Chinese Academy of Sciences, Beijing 100049, China*

Received: 9 November 2017
Revised: 6 December 2017
Accepted: 10 December 2017

KEYWORDS
CIGS solar cell,
pyro-phototronic effect,
piezo-phototronic effect,
piezopotential,
pyropotential

ABSTRACT

Cu(In, Ga)Se_2 (CIGS)-based materials have gained remarkable attention for thin-film photovoltaic applications due to their high absorption coefficient, tunable bandgap, compositional tolerance, outstanding stabilities, and high efficiency. A small increase in the efficiency of CIGS solar cells has huge economic impact and practical importance. As such, we fabricated a flexible CIGS solar cell on a mica substrate and demonstrated the enhanced device performance through the piezo- and pyro-phototronic effects based on a ZnO thin film. The device showed enhanced energy conversion efficiency from 13.48% to 14.23% by decreasing the temperature from 31 to 2 ˚C at a rate of ~ 0.6 ˚C·s^{-1} via the pyro-phototronic effect, and further enhanced from 14.23% to 14.37% via the piezo-phototronic effect by further applying a static compressive strain. A pyro-electric nanogenerator effect was also found to promote the performance of the CIGS solar cell at the beginning of the cooling process. The manipulated energy band of the CIGS/CdS/ZnO heterojunction under the influence of the inner pyroelectric and piezoelectric potentials is believed to contribute to these phenomena. Applying the piezo- and pyro-phototronic effects simultaneously offers a new opportunity for enhancing the output performance of commercial thin film solar cells.

1 Introduction

With the impending threat of energy shortage and deterioration of the environment, great efforts are being devoted to developing renewable and green energy resources. As such, converting energy effectively from other energy resources is becoming a crucial issue [1–3]. Among them, solar energy, which will provide a significant fraction of the world's energy needs over the next century, is attracting substantial interest due to its reliable, abundant, and sustainable nature [3–6]. In recent years, piezoelectric semiconductor thin films or nanowires have been used; they typically have a wurtzite structure (such as ZnO, CdS and GaN). The piezo-phototronic effect, a new mechanism that is used to modulate the behavior of photoexcited carriers and engineer new optoelectronic devices, operates via the coupling among piezoelectricity, semiconductor charge transport, and optical processes in piezoelectric semiconductors. Utilizing this mechanism

Address correspondence to zhong.wang@mse.gatech.edu

has proven to be an effective approach to improve the separation of photo-induced electron–hole pairs, suppress nonradiative recombination, and significantly enhance the performance of photovoltaic cells (PVCs) [7–16]. Upon normal stress, owing to the non-central symmetric crystal structure, the piezoelectric polarization charges together with the induced piezo-potential in the piezoelectric semiconductor at the heterojunction or interface can modulate the band structure of the heterojunction and tune the charge separation, transport, and recombination in optoelectronic processes. Consequently, the photo-current of the optoelectronic device is either enhanced or reduced, which is the working principle of the piezo-phototronic effect [7–9, 17]. However, the impact of the piezo-phototronic effect on commercial solar cells has not yet been investigated. Moreover, a novel working mechanism by coupling pyroelectricity, photoexcitation, and semiconductor characteristics, called the "pyro-phototronic effect", has recently been proposed in pyroelectric materials (which usually simultaneously possess piezoelectric characteristics) to significantly improve the generation, transport, separation, and/or recombination of photoinduced charge carriers, such as in the enhanced performance of heterojunction photodetectors or solar cells [18–20]. Actually, the pyroelectric-enhanced photovoltaic performance mainly arises from two aspects: the inner pyroelectric nanogenerator (PENG) and the PENG-induced band bending at the heterojunction. As piezo- and pyro-phototronic effects are both based on polarization charges, it is expected that they can be coupled for further enhancement of optoelectronic performance.

Recently, Cu(In, Ga)Se_2 (CIGS)-based materials have gained marked attention for thin-film photovoltaic applications due to their high absorption coefficient, tunable bandgap, compositional tolerance, outstanding stabilities, and high efficiency [21–24]. The efficiency of industrial CIGS technology is comparable to that of polycrystalline silicon technologies and may compete with single crystalline silicon technologies in the near future [25].

In this work, we developed a conventional flexible CIGS solar cell (see Fig. 1(a)). Using the piezo- and pyro-phototronic effects based on a ZnO thin film, the performance of the CIGS solar cell is effectively enhanced. The device shows an improvement of energy conversion efficiency from 13.48% to 14.23%

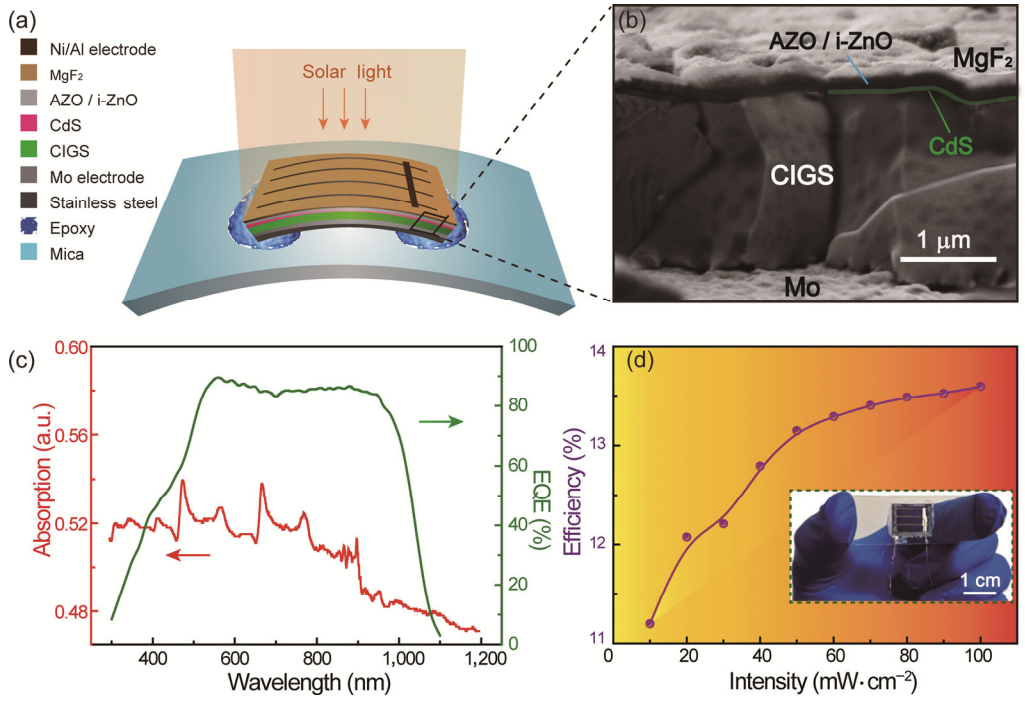

Figure 1 CIGS solar cell layout. (a) Schematic structure of the flexible solar cell under illumination. (b) Cross-sectional SEM image of the as-fabricated solar cell. (c) Absorption and external quantum efficiency spectra of the solar cell. (d) Solar energy conversion efficiency of the solar cell under AM 1.5G illumination. The inset is an optical image of the device.

by decreasing the temperature from 31 to 2 ℃ via the pyro-phototronic effect, and additional improvement from 14.23% to 14.37% via the piezo-phototronic effect by further applying a static compressive strain. Simultaneous application of the piezo- and pyro-phototronic effects offers a new opportunity for enhancing the output performance of commercial thin film solar cells.

2 Results and discussion

A 2 μm p-CIGS absorption layer was first grown on Mo-coated stainless steel (25 μm), and then followed in turn by a n-CdS buffer layer, intrinsic ZnO, n-type ZnO (AZO), MgF_2 anti-reflection layer and Ni/Al grids, which was then fixed on a 250 μm flexible mica substrate by epoxy (Fig. 1(a)). Figure 1(b) shows a cross-sectional scanning electron microscopy (SEM) image of the CIGS solar cell. For the detailed fabrication processes, please refer to the Methods part. Solar light with AM 1.5G spectral distribution was irradiated vertically on the surface of the CIGS solar cell. From the measurement of the absorption and external quantum efficiency (EQE) spectra (see Fig. 1(c)), we found that the bandgap of the CIGS absorber was ~ 1.12 eV and that the light absorption was mainly focused on the visible spectrum. As shown in Fig. 1(d), the efficiency at room temperature increased with the increase in light intensity and reaches up to ~ 13.5% under AM 1.5G (1 sun) illumination, which is the level of commercial solar cells. Furthermore, the efficiency was still maintained at a relatively high level with weak light intensity (for example, the efficiency is ~ 11.2% under 0.1 sun illumination). The CIGS solar cell could also be bended easily by applying a strain on the flexible mica. Notably, the mica used here also possessed good thermal conductivity, which was beneficial to the study of the pyro-phototronic effect.

To investigate the influence of the piezo-potential on the performance of such a thin film solar cell, the current (density)–voltage (*J*–*V*) characteristics of the solar cell under a variety of bending strains (from −0.62% to 0.55%) were measured under AM 1.5G illumination, as shown in Figs. 2(a) and 2(b). Here, the piezo-potential was derived from the preferred *c*-axis-oriented ZnO thin film grown via radio frequency magnetron sputtering, which has been proven by many researchers [26–28]. To our knowledge, no report has proven the piezoelectric performance for a CdS thin film grown by chemical bath deposition; hence, we will not consider the piezo-potential from CdS thin films in this study. The downward and upward bending of the mica substrate (with 250 μm in thickness) is equivalent to applying compressive and tensile strain on the CIGS sample, respectively. Regardless of the thickness of the CIGS solar cell layers, the compressive or tensile strain was calculated, which actually denoted the deformation of the top surface of the mica substrate. As shown in Fig. 2(b), the performance of such a PV device was enhanced slightly with an increase in the applied compressive strain but decreased with an increase in the applied tensile strain. Notably, the change in illumination angle and surface area due to the shape change of the substrate was considered according to the refraction law

$$n_1 \sin(\theta_1) = n_2 \sin(\theta_2) \quad (1)$$

and the dependence of the reflectivity on the incidence angle of natural sunlight

$$R_n = \frac{1}{2}\left[\frac{\sin^2(\theta_1-\theta_2)}{\sin^2(\theta_1+\theta_2)} + \frac{\tan^2(\theta_1-\theta_2)}{\tan^2(\theta_1+\theta_2)}\right] \quad (2)$$

where n_1 (= 1), n_2 (= 1.38), θ_1, θ_2, R_n are the refraction of air, refraction of MgF_2, incidence angle, refraction angle, and reflectivity for a natural sunlight, respectively. We found that the reflectivity almost stays constant for $\theta_1 < 45°$. Therefore, the change in performance due to the change of illumination angle could be ignored in our case. The performance of the solar cell could also be affected by a change in the effective illumination area due to the bending deformation. The effective illumination areas for the upward and downward bending of the device both decreased. If there is no piezo-potential in ZnO, the efficiency of the device will decrease for both upward and downward bending. We have normalized the efficiency in Fig. 2 considering the change in the effective illumination area. Specifically, J_{SC} and V_{OC} under different strains were extracted and plotted in Fig. 2(c). It was found that

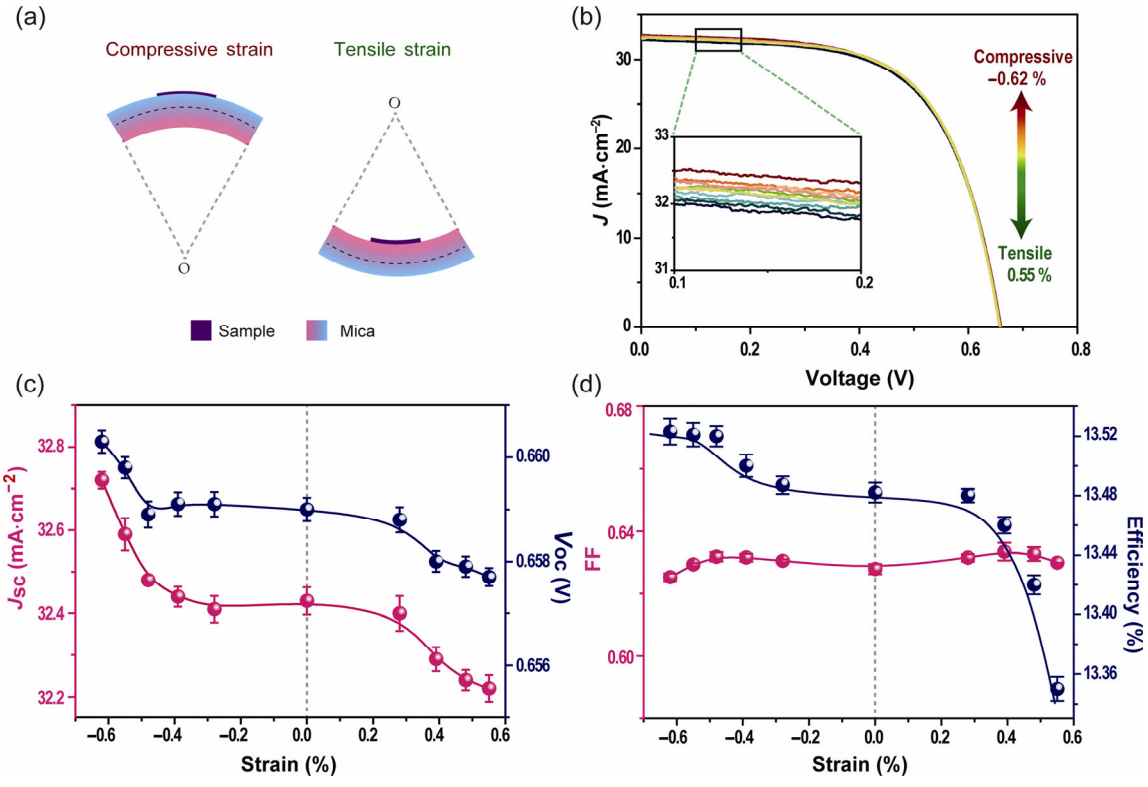

Figure 2 Performance of CIGS solar cell under strains at room temperature. (a) Schematic of the flexible solar cell under compressive and tensile strains. (b) *J*–*V* characteristics of the solar cell under different strains. (c) Strain dependence of the short-circuit current density (J_{SC}) and the open-circuit voltage (V_{OC}). (d) Strain dependence of the solar energy conversion efficiency (η) and the fill factor (FF).

the J_{SC} increased from 32.22 to 32.72 mA·cm^{-2} for a 1.6% variation, and that the V_{OC} increased from 0.657 to 0.66 V for a 0.46% fluctuation. The fill factor FF was about 0.63, which was almost invariable with a change of strain. As a result, the solar energy conversion efficiency was tuned from 13.35% to 13.53%. Such enhanced performance of the solar cell under a compressive strain was believed to be due to a modulation of the energy band caused by piezoelectric polarization charges at the heterojunction interface between ZnO and CdS [7, 8, 29–32], which will be discussed later.

The pyro-electric current and voltage can be described as

$$I = P_C A(\mathrm{d}T/\mathrm{d}t) \quad (3)$$

$$V = P_V \Delta T r_d \quad (4)$$

respectively, where P_C is the pyro-electric current coefficient, P_V is the pyro-electric voltage coefficient, A is the electrode area, $\mathrm{d}T/\mathrm{d}t$ is the rate of change in temperature, ΔT is the change in temperature, and r_d is the effective Debye length of pyro-electric materials (such as ZnO and CdS) [33]. Usually, the pyro-electric coefficient is defined as the differential change of spontaneous polarization due to a change in temperature. When the dimensions and volume of the material are fixed, the primary pyro-electric coefficient can be used to describe the charges produced under a change in temperature. If the material's dimensions/volume can change due to a change in temperature, strain will be induced due to the anisotropic deformation of the material, resulting in an additional contribution of piezoelectrically induced charges. It is commonly described as pyro-phototronic effect, a secondary pyro-electric effect, which is more important for wurtzite piezo-crystals (such as ZnO, CdS) [34–36].

We studied the influence of cooling and heating processes on the current–time characteristics of the PV device. The total photocurrent can be expressed as

$$J_{total} = J_{PV} + J_{PENG} + J_{pyro\text{-}ph} \quad (5)$$

where J_{PV}, J_{PENG}, and $J_{pyro\text{-}ph}$ are the currents corresponding to the photovoltaic effect, pyro-electric nanogenerator,

and pyro-phototronic effect, respectively. Figure 3(a) illustrates the variation of the applied temperature with time. As shown in Fig. 3(b), the photocurrent increased rapidly from zero to 15.68 mA·cm^{-2} with the light (1 sun) illumination switching on, and the photocurrent further increased when a 2 ˚C cooling process was applied at a rate of ~ 0.6 ˚C·s^{-1} because of the current of the pyro-electric nanogenerator, pyro-phototronic effect due to tuning of the energy band via polarized charges in the ZnO thin film, and enhanced relaxation time for the photo-generated carriers. The photocurrent was enhanced by ~ 17% at the beginning of the cooling process and by ~ 7% at the end of the cooling process. The photocurrent decreased sharply and remained at ~ 15.68 mA·cm^{-2} when the cooling process ended, which further decreased rapidly to zero with the light illumination switching off. On the contrary, a reversed pyro-electric potential was generated when a 58 ˚C heating process was applied due to an opposing pyro-electric current, reversed pyro-phototronic effect, and reduced relaxation time of photo-generated carriers, as shown in Fig. 3(c). Although the total current density is expressed in Eq. (5), J_{PENG} could only operate at the very beginning of the cooling process. In Fig. 3, the current–time characteristics were measured under a fixed voltage of 0.6 V. In this case, the J_{PENG} would contribute little with the passage of time, which might be negligible. However, the $J_{pyro\text{-}ph}$ will be enhanced during the cooling process. With the temperature gradient decreasing gradually to zero, the $J_{pyro\text{-}ph}$ could work even more efficiently.

The influence of a 2 ˚C cooling process at a rate of ~ 0.6 ˚C·s^{-1} and a −0.65% compressive strain on the *J*–*V* characteristics of the solar cell is shown in Fig. 4. The efficiency was ~ 13.48% without the strain and cooling process, which increased to ~ 14.23% only with a cooling process from 31 to 2 ˚C. Moreover, it was further enhanced to ~ 14.37% with both a 2 ˚C cooling process and a −0.65% compressive strain. Notably, there is no PENG current flowing in the circuit in this measurement, since the charge polarization was constant at a stable temperature. Next, we will analyze the observed phenomena through the viewpoint of the energy band.

The piezoelectric and pyroelectric effects that enhanced the photovoltaic performance of the CIGS solar cell can be explained from the bending energy band of the CIGS/CdS/ZnO heterojunction under the influence of the inner pyroelectric and piezoelectric potentials. For the i-ZnO, n-CdS, and p-CIGS used in this work, the band gaps are 3.2, 2.42, and 1.159 eV, respectively, and the electron affinities are 4.2, 4.5, and 4.202 eV, respectively. The energy band in the free condition can be drawn as Fig. 5(a). When only a compressive strain was applied to the device, due to the *c*-axis polar orientation in ZnO, the piezo-potential spreads along the ZnO layer with positive and negative piezoelectric polarization charges appearing at the right and left sides of the ZnO thin film, respectively (see Fig. 5(b)). Consequently, the energy level of the depletion zone was further decreased especially at the hetero-interface with positive charges, while the energy level for negative charges increased. Therefore, the trapped

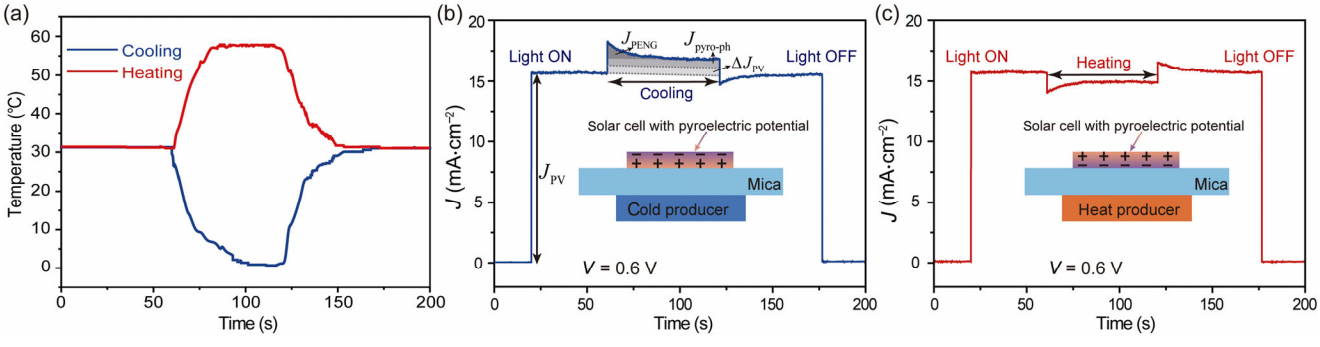

Figure 3 The performance of the solar cell with a cooling or heating processes. (a) The variation of the applied temperature with time. (b) Influence of cooling process with the rate of ~ 0.6 ˚C·s^{-1} on the current–time characteristics of the PV device with a fixed voltage of 0.6 V and 1 sun light illumination. (c) Influence of heating process on the current–time characteristics of the PV device with a fixed voltage of 0.6 V and 1 sun light illumination.

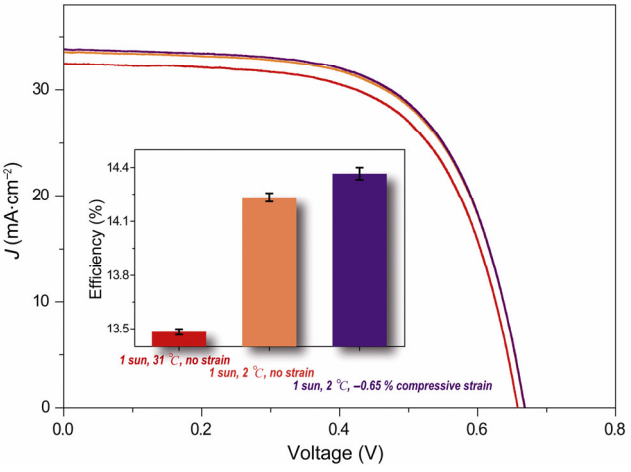

Figure 4 Influence of the cooling process and compressive strain on the *J*–*V* characteristics of the solar cell, with the inset denoting the efficiency of the three cases.

photo-generated electrons in the ZnO/CdS interface were released into n-ZnO (Fig. 5(b)), which enhanced the photovoltaic performance of the CIGS solar cell as shown in Fig. 2(d). The open-circuit voltage V_{OC} and the reverse saturation current I_0 can be expressed as

$$V_{OC} = \frac{k_0 T}{e} \ln\left(\frac{I_{sc}}{I_0}\right) \tag{6}$$

$$I_0 = I_{00} \exp\left(-\frac{\Delta E}{r k_0 T}\right) \tag{7}$$

where I_{SC} is the short-circuit current, I_{00} is a prefactor, r is an ideality factor, and ΔE is the energy band difference between the conduction band of an n-type inorganic material and conduction band of a p-type inorganic material [14]. By combining Eqs. (6) and (7), the open-circuit voltage V_{OC} can be further expressed by

$$eV_{OC} = \frac{1}{r}\Delta E + k_0 T \ln\left(\frac{I_{sc}}{I_{00}}\right) \tag{8}$$

which indicates that the open-circuit voltage V_{OC} is associated with both the energy band difference ΔE and short-circuit current I_{SC}, regardless of the change in ΔE with the increase of compressive strain. The change of V_{OC} with strain and temperature cannot be illustrated from Fig. 5 as it was a combined effect due to the variation of the temperature and the short-circuit current in Eq. (8). The fill factor FF was almost invariable under strain as shown in Fig. 2(d), which might be due to the invariable series resistance and shunt resistance in the solar cell system. On the

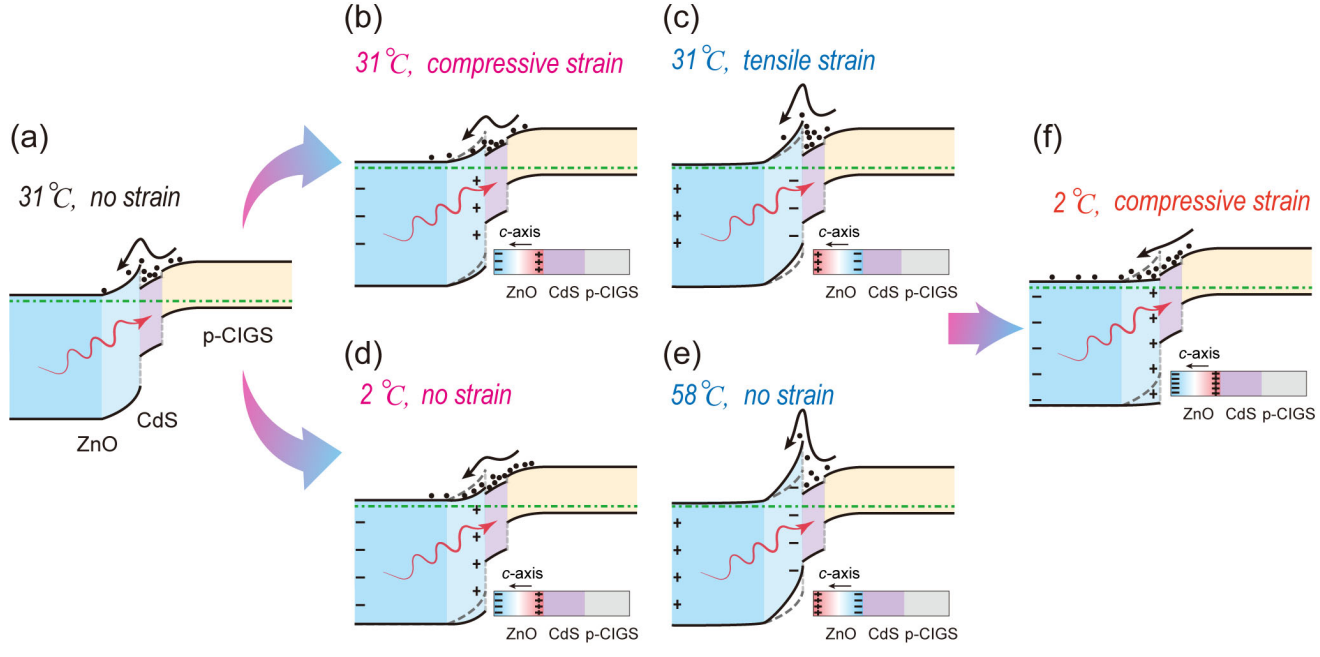

Figure 5 Schematic diagrams of the energy bands under different temperatures and strains. (a), (b), and (c) Band diagrams at the temperature of 31 ˚C under zero, compressive, and tensile strains, respectively. (d) and (e) Band diagrams under zero strain with cooling and heating processes, respectively. (f) Band diagram under compressive strain and with a cooling process from 31 to 2 ˚C with a rate of ~ 0.6 ˚C·s^{-1}.

contrary, when only a tensile strain was applied on the device, the number of trapped photo-generated electrons in ZnO/CdS interface would increase (see Fig. 5(c)); therefore, the photovoltaic performance of the CIGS solar cell was weakened as shown in Fig. 2(d). When the device was only subjected to a decrease in temperature from 31 to 2 ℃, the pyro-potential spreads along ZnO with positive and negative piezoelectric polarization charges appearing at the right and left sides of ZnO, respectively (see Fig. 5(d)), which resulted in an enhancement of photovoltaic performance, similar to the case in Fig. 5(b). However, the cooling process herein contributed more to the enhanced performance of the CIGS solar cell than the applied compressive strain in Fig. 5(b), which was mainly due to the stronger pyro-phototronic effect or increased lifetime of photo-generated carriers at lower temperature. Distinguishing which one was dominant was difficult with regard to the pyro-phototronic effect and carrier lifetime. On the contrary, when the device was only subjected to an increase in temperature from 31 to 58 ℃, the number of trapped photo-generated electrons in the ZnO/CdS interface would increase (see Fig. 5(e)); therefore, the photovoltaic performance of the CIGS solar cell weakened, as shown in Fig. 2(d). When the cooling process and compressive strain are applied on the device simultaneously, the pyro-potential and piezo-potential would stack together, which can greatly lower the energy level at the hetero-interface with positive charges and greatly raise the energy level at the hetero-interface with negative charges. Therefore, the trapped photo-generated electrons in ZnO/CdS interface would be released into n-ZnO more easily (Fig. 5(f)), which further enhanced the photovoltaic performance of the CIGS solar cell as shown in Fig. 4.

3 Conclusions

A flexible CIGS solar cell was fabricated. The device maintained a relatively high efficiency even with weak light intensity. The efficiency could be tuned simply via bending the mica substrate. The device efficiency was enhanced from 13.48% to 14.23% by decreasing the temperature from 31 to 2 ℃ at a rate of ~ 0.6 ℃·s^{-1} via the pyro-phototronic effect, and was further enhanced from 14.23% to 14.37% via the piezo-phototronic effect by further applying a static compressive strain. The effectively enhanced performance of the CIGS solar cell is believed to be due to the piezo- and pyro-phototronic effects based on the ZnO thin film. The PENG effect could also enhance the performance of the CIGS solar cell at the beginning of cooling process. Finally, we explained the results from the modulated energy bands of the CIGS/CdS/ZnO heterojunction under the influence of the inner pyroelectric and piezoelectric potentials. Applying the piezo- and pyro-phototronic effects simultaneously offers a new opportunity for enhancing the output performance of commercial thin film solar cells.

4 Methods

4.1 Fabrication processes of the solar cells

A CIGS absorber (2 μm, Ga/(Ga + In) = 0.3, SUN HARMONICS) was grown on a stainless steel substrate (25 μm, SUS301(1Cr17Ni7), TAIYUAN IRON&STEEL (GROUP) CO., LTD.) with direct-current (DC)-sputtered Mo back contact (1 μm, 99.95%, www.znxc.cn). The CIGS films were then covered with CdS (SUN HARMONICS) of a thickness in the range of 50–70 nm by chemical bath deposition. A 90-nm thick i-ZnO (99.995%) layer was first deposited, and then the ZnO:Al (doping density 2.5%) layers, with a thickness of 350 nm and sheet resistance of approximately 50 Ω·square^{-1}, were deposited by radio frequency (RF) magnetron sputtering. Sputtering the undoped layer in ambient oxygen ensured high transmission and resistivity. 50-nm Ni/3-μm Al grids were deposited respectively by electron beam evaporation. A 100-nm thick MgF_2 (99.99%) film was deposited to serve as an anti-reflection coating. The cell edges were etched in diluted hydrochloric acid (3 M) for 5 min to avoid the short-circuit of the devices. The total area of the cells is ~ 1 cm^2. Then, the cells were fixed on mica substrates (250 μm in thickness) by epoxy.

4.2 Characterization and measurement

The detailed microscopic structural and morphological characterizations were carried out with a HITACHI SU8020 field-emission scanning electron microscope (FESEM). The absorption spectra were obtained

with a UV-VIS-NIR spectrophotometer (SHIMADZU UV3600). The solar cells were irradiated using a solar simulator (Model 94023A, Newport) with an AM 1.5G spectrum distribution calibrated against a NREL reference cell to accurately simulate the full solar intensity (100 mW·cm^{-2}). The external quantum efficiency spectra were measured by a quantum efficiency measurement system (QEPVSI-b, Newport). The thermoelectric-based cooler and heater were used to change the temperature of the device. A temperature sensor was used to record the temperature of the CIGS thin film. Two three-dimensional manual displacement stages were applied to bend the device. The current–voltage and current–time characteristics of the devices were recorded by an electrochemical workstation (CHI660E).

Acknowledgements

This research was supported by the "thousands talents" program for pioneer researcher and his innovation team, China, National Natural Science Foundation of China (Nos. 11704032, 51432005, 5151101243, and 51561145021), the National Key R&D Project from Ministery of Science and Technology (No. 2016YFA0202704), the National Program for Support of Top-notch Young Professionals, and the China Postdoctoral Science Foundation (No. 2016M600067).

References

[1] Zhang, Y.; Yang, Y.; Gu, Y. S.; Yan, X. Q.; Liao, Q. L.; Li, P. F.; Zhang, Z.; Wang, Z. Z. Performance and service behavior in 1-D nanostructured energy conversion devices. *Nano Energy* **2015**, *14*, 30–48.

[2] Yu, Y. H.; Zhang, Z.; Yin, X.; Kvit, A.; Liao, Q. L.; Kang, Z.; Yan, X. Q.; Zhang, Y.; Wang, X. D. Enhanced photoelectrochemical efficiency and stability using a conformal TiO_2 film on a black silicon photoanode. *Nature Energy* **2017**, *2*, 17045.

[3] Tyagi, V. V.; Rahim, N. A. A.; Rahim, N. A.; Selvaraj, J. A. L. Progress in solar PV technology: Research and achievement. *Renew. Sust. Energy Rev.* **2013**, *20*, 443–461.

[4] Polman, A.; Knight, M.; Garnett, E. C.; Ehrler, B.; Sinke, W. C. Photovoltaic materials: Present efficiencies and future challenges. *Science* **2016**, *352*, aad4424.

[5] Kraemer, D.; Poudel, B.; Feng, H. P.; Caylor, J. C.; Yu, B.; Yan, X.; Ma, Y.; Wang, X. W.; Wang, D. Z.; Muto, A. et al. High-performance flat-panel solar thermoelectric generators with high thermal concentration. *Nat. Mater.* **2011**, *10*, 532–538.

[6] Ni, G.; Li, G.; Boriskina, S. V.; Li, H. X.; Yang, W. L.; Zhang, T. J.; Chen, G. Steam generation under one sun enabled by a floating structure with thermal concentration. *Nat. Energy* **2016**, *1*, 16126.

[7] Wang, Z. L. Piezopotential gated nanowire devices: Piezotronics and piezo-phototronics. *Nano Today* **2010**, *5*, 540–552.

[8] Wang, Z. L. Progress in piezotronics and piezo-phototronics. *Adv. Mater.* **2012**, *24*, 4632–4646.

[9] Wu, W. Z.; Wang, Z. L. Piezotronics and piezo-phototronics for adaptive electronics and optoelectronics. *Nat. Rev. Mater.* **2016**, *1*, 16031.

[10] Wang, Z. L. Piezo-phototronic effect on solar cells. In *Piezotronics and Piezo-Phototronics*. Springer: Berlin, Heidelberg, 2012; pp153–178.

[11] Hu, G. F.; Guo, W. X.; Yu, R. M.; Yang, X. N.; Zhou, R. R.; Pan, C. F.; Wang, Z. L. Enhanced performances of flexible ZnO/perovskite solar cells by piezo-phototronic effect. *Nano Energy* **2016**, *23*, 27–33.

[12] Pan, C. F.; Niu, S. M.; Ding, Y.; Dong, L.; Yu, R. M.; Liu, Y.; Zhu, G.; Wang, Z. L. Enhanced Cu_2S/CdS coaxial nanowire solar cells by piezo-phototronic effect. *Nano Lett.* **2012**, *12*, 3302–3307.

[13] Yang, Y.; Guo, W. X.; Zhang, Y.; Ding, Y.; Wang, X.; Wang, Z. L. Piezotronic effect on the output voltage of P_3HT/ZnO micro/nanowire heterojunction solar cells. *Nano Lett.* **2011**, *11*, 4812–4817.

[14] Zhu, L. P.; Wang, L. F.; Xue, F.; Chen, L. B.; Fu, J. Q.; Feng, X. L.; Li, T. F.; Wang, Z. L. Piezo-phototronic effect enhanced flexible solar cells based on n-ZnO/p-SnS core–shell nanowire array. *Adv. Sci.* **2017**, *4*, 1600185.

[15] Zhang, Y.; Yang, Y.; Wang, Z. L. Piezo-phototronics effect on nano/microwire solar cells. *Energy Environ. Sci.* **2012**, *5*, 6850–6856.

[16] Zhu, L. P.; Wang, L. F.; Pan, C. F.; Chen, L. B.; Xue, F.; Chen, B. D.; Yang, L. J..; Su, L.; Wang, Z. L. Enhancing the efficiency of silicon-based solar cells by the piezo-phototronic effect. *ACS Nano* **2017**, *11*, 1894–1900.

[17] Zhang, Z.; Kang, Z.; Liao, Q. L.; Zhang, X. M.; Zhang, Y. One-dimensional ZnO nanostructure-based optoelectronics. *Chin. Phys. B* **2017**, *26*, 118102.

[18] Wang, Z. N.; Yu, R. M.; Pan, C. F.; Li, Z. L.; Yang, J.; Yi, F.; Wang, Z. L. Light-induced pyroelectric effect as an effective approach for ultrafast ultraviolet nanosensing. *Nat. Commun.* **2015**, *6*, 8401.

[19] Zhang, K. W.; Wang, Z. L.; Yang, Y. Enhanced P_3HT/ZnO nanowire array solar cells by pyro-phototronic effect. *ACS Nano* **2016**, *10*, 10331–10338.

[20] Peng, W. B.; Yu, R. M.; Wang, X. N.; Wang, Z. N.; Zou, H. Y.; He, Y. N.; Wang, Z. L. Temperature dependence of pyro-phototronic effect on self-powered ZnO/perovskite heterostructured photodetectors. *Nano Res.* **2016**, *9*, 3695–3704.

[21] Ramanathan, K.; Contreras, M. A.; Perkins, C. L.; Asher, S.; Hasoon, F. S.; Keane, J.; Young, D.; Romero, M.; Metzger, W.; Noufi, R. et al. Properties of 19.2% efficiency ZnO/CdS/$CuInGaSe_2$ thin-film solar cells. *Prog. Photovoltaics: Res. Appl.* **2003**, *11*, 225–230.

[22] Chirilă, A.; Buecheler, S.; Pianezzi, F.; Bloesch, P.; Gretener, C.; Uhl, A. R.; Fella, C.; Kranz, L.; Perrenoud, J.; Seyrling, S. et al. Highly efficient $Cu(In,Ga)Se_2$ solar cells grown on flexible polymer films. *Nat. Mater.* **2011**, *10*, 857–861.

[23] Repins, I.; Contreras, M. A.; Egaas, B.; DeHart, C.; Scharf, J.; Perkins, C. L.; To, B.; Noufi, R. 19.9%-efficient ZnO/CdS/$CuInGaSe_2$ solar cell with 81.2% fill factor. *Prog. Photovoltaics: Res. Appl.* **2008**, *16*, 235–239.

[24] Aé, L.; Kieven, D.; Chen, J.; Klenk, R.; Rissom, T.; Tang, Y.; Lux-Steiner, M. C. ZnO nanorod arrays as an antireflective coating for $Cu(In,Ga)Se_2$ thin film solar cells. *Prog. Photovoltaics: Res. Appl.* **2010**, *18*, 209–213.

[25] Duchatelet, A.; Letty, E.; Jaime-Ferrer, S.; Grand, P. P.; Mollica, F.; Naghavi, N. The impact of reducing the thickness of electro-deposited stacked Cu/In/Ga layers on the performance of CIGS solar cells. *Sol. Energy Mater. Sol. C.* **2017**, *162*, 114–119.

[26] Wen, X. N.; Wu, W. Z.; Wang, Z. L. Effective piezo-phototronic enhancement of solar cell performance by tuning material properties. *Nano Energy* **2013**, *2*, 1093–1100.

[27] Wen, X. N.; Wu, W. Z.; Ding, Y.; Wang, Z. L. Piezotronic effect in flexible thin-film based devices. *Adv. Mater.* **2013**, *25*, 3371–3379.

[28] Li, C. P.; Yang, B. H. Local piezoelectricity and polarity distribution of preferred c-axis-oriented ZnO film investigated by piezoresponse force microscopy. *J. Electron. Mater.* **2011**, *40*, 253–258.

[29] Zhang, F.; Ding, Y.; Zhang, Y.; Zhang, X. L.; Wang, Z. L. Piezo-phototronic effect enhanced visible and ultraviolet photodetection using a ZnO–CdS core–shell micro/nanowire. *ACS Nano* **2012**, *6*, 9229–9236.

[30] Zhang, Z.; Liao, Q. L.; Yu, Y. H.; Wang, X. D.; Zhang, Y. Enhanced photoresponse of ZnO nanorods-based self-powered photodetector by piezotronic interface engineering. *Nano Energy* **2014**, *9*, 237–244.

[31] Zhang, Y.; Yan, X. Q.; Yang, Y.; Huang, Y. H.; Liao, Q. L.; Qi, J. J. Scanning probe study on the piezotronic effect in ZnO nanomaterials and nanodevices. *Adv. Mater.* **2012**, *24*, 4647–4655.

[32] Lin, P.; Gu, Y. S.; Yan, X. Q.; Lu, S. N.; Zhang, Z.; Zhang, Y. Illumination-dependent free carrier screening effect on the performance evolution of ZnO piezotronic strain sensor. *Nano Res.* **2016**, *9*, 1091–1100.

[33] Yang, Y.; Wang, S. H.; Zhang, Y.; Wang, Z. L. Pyroelectric nanogenerators for driving wireless sensors. *Nano Lett.* **2012**, *12*, 6408–6413.

[34] Yang, Y.; Guo, W. X.; Pradel, K. C.; Zhu, G.; Zhou, Y. S.; Zhang, Y.; Hu, Y. F.; Lin, L.; Wang, Z. L. Pyroelectric nanogenerators for harvesting thermoelectric energy. *Nano Lett.* **2012**, *12*, 2833–2838.

[35] Ye, C. P.; Tamagawa, T.; Polla, D. L. Experimental studies on primary and secondary pyroelectric effects in $Pb(Zr_xTi_{1-x})O_3$, $PbTiO_3$, and ZnO thin films. *J. Appl. Phys.* **1991**, *70*, 5538–5543.

[36] Zook, J. D.; Liu, S. T. Pyroelectric effects in thin film. *J. Appl. Phys.* **1978**, *49*, 4604–4606.